RSC Advances

ROYAL SOCIETY OF CHEMISTRY

PAPER

View Article Online
View Journal | View Issue

Check for updates

Cite this: *RSC Adv.*, 2025, **15**, 2462

Cu/Cu$_2$O/NH$_2$-MIL-88B (Fe) heterojunction as the photocatalyst to remove hexavalent chromium heavy metal ions in water†

Chunhua Xu

Received 18th November 2024
Accepted 21st January 2025

DOI: 10.1039/d4ra08143a

rsc.li/rsc-advances

This work aimed at addressing the problem of hexavalent chromium pollution in the water environment, designing and preparing the Cu/Cu$_2$O/NH$_2$-MIL-88B (Fe) heterojunction material with NH$_2$-MIL-88B (Fe) as the carrier, Cu/Cu$_2$O was loaded on NH$_2$-MIL-88B (Fe) by light-assisted reduction. The loading of Cu$_2$O effectively improves the visible light absorption capacity of the composite material. The SPR effect of Cu improves the separation and transfer of photogenerated carriers in the composite material. Performance test results showed that under the condition of pH = 2, using ethanol as a sacrificial agent, Cu/Cu$_2$O/NH$_2$-MIL-88B (Fe) (15 wt%) had a photocatalytic adsorption reduction rate of Cr(VI) of 96.3% in 60 minutes of adsorption in the dark and 150 minutes of photocatalytic reduction, which was 1.39 times that of NH$_2$-MIL-88B (Fe). In addition, the composite material had good stability and recyclability, and the reduction efficiency still reached 88.9% after three cycles.

1. Introduction

With the rapid development of industry, more and more water-soluble pollutants such as heavy metal ions flow into the water environment, and human health and the sustainable development of society are facing serious threats.[1] Many countries have introduced relevant policies for water environment protection, such as the "Federal Water Policy" issued by the Canadian federal government in 1987, the "EU Water Framework Directive" issued by the European Union in 2000, and the "Water Law of the People's Republic of China" promulgated by China in 2002. Hexavalent chromium (Cr(VI)), as a typical heavy metal ion, has the characteristics of toxicity, carcinogenicity, high solubility and high mobility.[2] After being absorbed by the human body, it can cause tympanic membrane perforation, lung cancer and liver cancer and other health problems.[3] Therefore, the effective removal of Cr(VI) in water is an environmental problem requiring to be solved urgently.[4] Chromium ions usually exist in two oxidation states: Cr(VI) and Cr(III).[5] Compared with the highly toxic Cr(VI), Cr(III) is not only less toxic, but also one of the essential trace elements for the human body.[6,7] It can be removed from water by forming a solid precipitate.[8] Therefore, reducing Cr(VI) to Cr(III) by reduction is an effective method for treating Cr(VI)-containing wastewater.[9]

Traditional reduction methods have found limited application due to their shortcomings such as low efficiency and secondary pollution.[10] In contrast, the photocatalytic reduction method has the advantages of environmental protection, simple reaction conditions and low cost, and is considered to be an effective way to treat Cr(VI)-containing wastewater.[11] The photocatalyst is at the core of photocatalytic technology.[12]

Metal–organic frameworks (MOFs) and covalent organic frameworks (COFs) have garnered considerable attention from research groups for their potential applications in photocatalysis.[13] MOFs are crystalline porous solid materials composed of central metals and organic ligands, which have the advantages of diverse types, adjustable structures, and large specific surface areas, and are very promising photocatalysts.[14] The catalytic reaction process of MOFs is related to the Ligand to Metal Charge Transfer (LMCT) process: under incident light irradiation, the organic ligand transfers the photogenerated electrons (e^-) generated by the transition to the central metal, forming a photogenerated carrier.[15,16] The streamer then undergoes a reduction or oxidation reaction. Therefore, reasonable modification of the central metal and organic ligands will effectively regulate the physical and chemical properties of MOFs.[17] He *et al.* synthesized Ti$_3$C$_2$/UiO-66-NH$_2$ composites with different proportions of Ti$_3$C$_2$ by an *in situ* solvothermal method and used them to enhance the photocatalytic removal of Cr(VI) for the first time. With suitable band positions and enhanced charge separation ability, the optimized sample Cr$_2$O$_7$$^{2-}$ photoreduction efficiency reaches 100% within 40 min.[18] Wang *et al.* integrated the synthesized intense visible-light absorption porphyrin unit and strong toxic anions adsorption strut into one single MOF simultaneously *via* a sequential mixed-ligand and ionization method, which strongly improved the photoreduction performance of Cr(VI). The synergistic effect of strong adsorption of Cr$_2$O$_7$$^{2-}$ and efficient

---

Dalian Vocational & Technical College (Dalian Radio and TV University), Dalian, 116035, P. R. China. E-mail: xuchunhua0331@163.com

† Electronic supplementary information (ESI) available. See DOI: https://doi.org/10.1039/d4ra08143a

utilization of light endowed $H_2TCPP \subset (I^-)$Meim-UiO-66 with highly efficient photoreduction activity toward toxic $Cr_2O_7^{2-}$ under visible light at a rate of 13.3 $mg_{Cr(VI)}\ g_{catalyst}^{-1}\ min^{-1}$.[19]

Fe is an environmentally friendly and highly abundant element.[20] At the same time, Fe–O clusters have visible light responsiveness.[21] Therefore, Fe-MOFs is a promising photocatalyst. Amino functionalization is an effective way to modify organic ligands.[22] For example, Shi *et al.*[23] investigated the effect of amino functionalization of MIL-88B (Fe), MIL-53 (Fe) and MIL-101 (Fe) on the excellent performance of reducing Cr(VI) under visible light. The results showed that modified organic linker could flexibly adjust its light collection efficiency. After the functionalization of the three MOFs amino groups, they all showed stronger responsiveness in the visible light region, thus improved the photocatalytic reduction effect of Cr(VI) in water. Therefore, Fe-MOFs functionalized with amino groups such as NH_2-MIL-88B (Fe) are effective catalysts for the treatment of chromium-containing wastewater.

Although MOFs are a potential material for treating Cr(VI)-containing wastewater,[24] there still some shortcomings such as weak visible light response and easy recombination of electron–hole pairs limit their application.[25] The formation of a composite photocatalyst by supporting the metal/metal-oxide on the MOFs through the heterostructure has proven to be an effective solution.[26] Metal nanoparticles such as Pd, Ag or Cu can form a rectifying Schottky barrier,[27] which is conducive to carrier separation. In contrast, Cu, as a transition element with surface plasmon resonance (SPR) effect,[28] has the advantages of good light response capability, high natural abundance and low price.[29] Cu_2O is a p-type metal oxide semiconductor material, which has the advantages of low band gap, short electron migration path, and good photosensitivity.[30] The formation of a heterostructure catalyst between Cu/Cu_2O and NH_2-MIL-88B (Fe) is beneficial to increase the light response range, improve the visible light absorption capacity, and at the same time promote the separation and transfer of photo-generated electron–hole pairs. This is beneficial to the treatment of Cr(VI) in wastewater.

Herein, the Cu/Cu_2O/NH_2-MIL-88B (Fe) heterostructure was designed and prepared through with NH_2-MIL-88B (Fe) as the carrier, Cu/Cu_2O was loaded on NH_2-MIL-88B (Fe) by light-assisted reduction method. The introduction of Cu/Cu_2O not only improved the visible light absorption capacity, but also promoted the separation and transfer of photogenerated electron–hole pairs, thereby improving the photocatalytic reduction efficiency of Cr(VI). A series of characterization methods were used to analyze the physical and chemical properties of Cu/Cu_2O/NH_2-MIL-88B (Fe) and speculate the possible mechanism.

2. Experimental section

The preparation of NH_2-MIL-88B (Fe) refers to the literature preparation method.[31] Dissolve 0.57 g $FeCl_3 \cdot 6H_2O$ and 0.32 g NH_2-BDC in 60 mL DMF, stir for 20 min, and then transfer to the reaction of PTFE lining. In the kettle, react at 170 °C for 15 h; after the high temperature reaction, transfer the solid product to an Erlenmeyer flask and continue to stir with methanol for 3 d; then, the solid product is washed, centrifuged, and finally vacuum dried at 50 °C for 5 h. A reddish brown solid product was obtained.

The preparation of Cu/Cu_2O/NH_2-MIL-88B (Fe) adopts the photo-assisted reduction method: a certain amount of $Cu(NO_3)_2$ solid is transferred to a beaker containing 60 mL of ethanol, and then 0.1 g of the above-prepared NH_2-MIL-88B (Fe) is added, kept stirring in the dark for 2 h, then irradiated with ultraviolet light for 2 h, and then centrifuged to obtain a solid product of Cu/Cu_2O/NH_2-MIL-88B (Fe). The preparation flow chart of Cu/Cu_2O/NH_2-MIL-88B (Fe) is shown in Scheme 1.

3. Results and discussions

3.1 Chemical and physical properties of Cu/Cu_2O/NH_2-MIL-88B (Fe)

Fig. 1 showed the XRD spectra of NH_2-MIL-88B (Fe) and Cu/Cu_2O/NH_2-MIL-88B (Fe). The XRD spectrum of NH_2-MIL-88B (Fe) was similar to the work of Yuan *et al.*[32] The characteristic

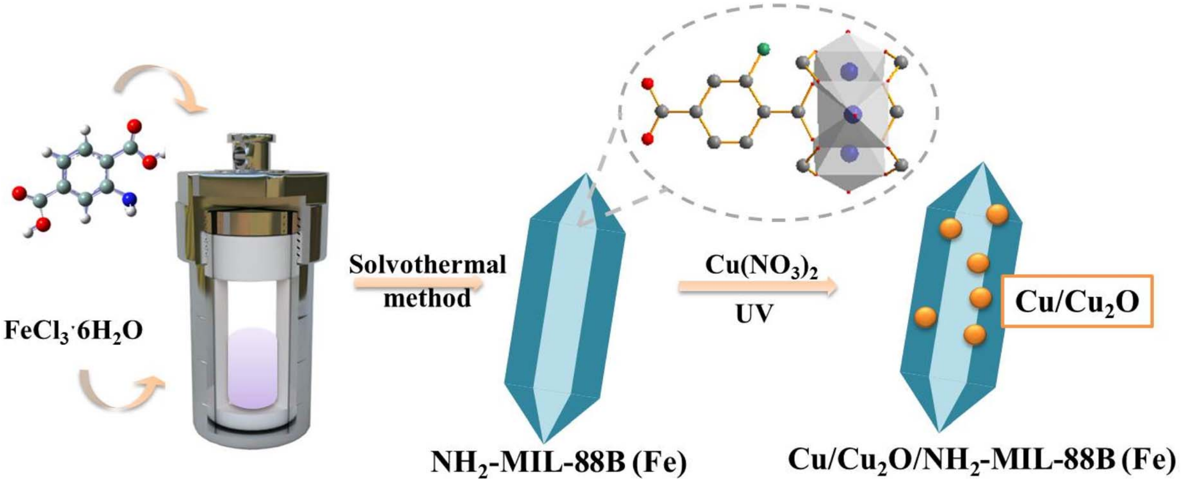

Scheme 1 Diagram of the synthetic processes of Cu/Cu_2O/NH_2-MIL-88B (Fe).

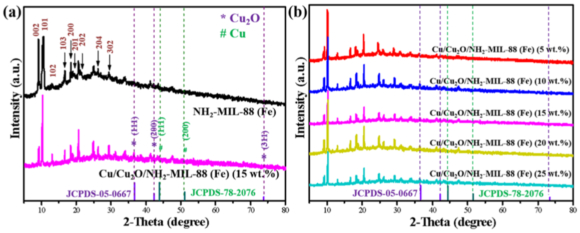

Fig. 1 XRD spectra of NH_2-MIL-88B (Fe) and Cu/Cu_2O/NH_2-MIL-88B (Fe) (a) and Cu/Cu_2O/NH_2-MIL-88B (Fe) with different loadings (b).

peaks corresponding to crystal planes such as (002), (101), (102), (103), (200), (201), (202), (204) and (302) of NH_2-MIL-88B (Fe) were consistent with the characteristic peaks of the simulation data (Cambridge Crystallographic Data Centre (CCDC) 647646),[33] which proved that NH_2-MIL-88B (Fe) was synthesized successfully. In the Cu/Cu_2O/NH_2-MIL-88B (Fe) in Fig. 1(a), the diffraction peaks at 36.5°, 42.2° and 73.9° were attributed to the crystal plane (111), (200) and (311) of Cu_2O (JCPDS-05-0667),[34] and the diffraction peaks at 43.6° and 50.6° were attributed to the Cu (111) and (200) crystal planes (JCPDS-78-2076),[35] which could preliminarily prove the formation of Cu/Cu_2O. In addition, the XRD pattern of Cu/Cu_2O/NH_2-MIL-88B (Fe) was consistent with the XRD pattern of NH_2-MIL-88B (Fe) except for Cu/Cu_2O, which indicated that NH_2-MIL-88B (Fe) maintained the crystal structure during the loading process of Cu/Cu_2O. The XRD characterization results preliminarily indicated that Cu/Cu_2O/NH_2-MIL-88B (Fe) had been successfully prepared. In addition, the low diffraction peaks of Cu/Cu_2O in Fig. 1(b)were due to the low content and uniform dispersion of Cu/Cu_2O nanoparticles supported on porous NH_2-MIL-88B (Fe).

Fig. 2 showed the FT-IR spectrum of the catalyst. Fig. 2(a) showed the spectra of organic ligands NH_2-BDC, NH_2-MIL-88B (Fe) and Cu/Cu_2O/NH_2-MIL-88B (Fe). Among them, 3454 cm^{-1} and 3376 cm^{-1} were attributable to the asymmetric and symmetric stretching vibrations of N–H of the $-NH_2$. It could be observed that these peaks were more obvious in the spectrum of NH_2-BDC than in MOFs, which may be related to the overlap of the characteristic –OH bands of adsorbed water near 3400 cm^{-1}. The flexural vibration absorption peak at 1625 cm^{-1} could be attributed to N–H, and the stretching vibration absorption peak at 1251 cm^{-1} could be attributed to C–N in aromatic amines, which showed that $-NH_2$ was maintained during the preparation of NH_2-MIL-88B (Fe) and Cu/Cu_2O/NH_2-MIL-88B (Fe). The region vibration between 1800–1100 cm^{-1} was related to –COOH,[31] –C═O and the benzene ring skeleton. The absorption peak at 1704 cm^{-1} was attributed to the stretching vibration absorption peak of –COOH. It was clearly observed that the absorption peak of NH_2-BDC was strong, while NH_2-MIL-88B (Fe) and Cu/Cu_2O/NH_2-MIL-88B (Fe) appeared as weak shoulder peaks or even disappear, which could be attributed to the polymerization reaction between –COOH in the organic ligand and the central metal precursor. The C═C stretching vibration absorption peaks of the benzene skeleton were at 1572 cm^{-1} and 1331 cm^{-1}. 768 cm^{-1} was attributed to the C–H flexural vibration absorption peak on the benzene. The position at 542 cm^{-1} was related to Fe–O vibration. It could be observed that there was no Fe–O peak in NH_2-BDC, while Fe–O peak was obviously generated in NH_2-MIL-88B (Fe) and Cu/Cu_2O/NH_2-MIL-88B (Fe). It was mutually corroborated by the weakening or disappearance of the above-mentioned characteristic absorption peak of the carboxyl group, indicated that NH_2-MIL-88B (Fe) and Cu/Cu_2O/NH_2-MIL-88B (Fe) produced structure of MOFs. The fingerprint absorption at 400–650 nm was the absorption peak of Cu_2O,[36] and the absorption centered at 700–900 nm was the absorption peak of Cu^0. However, due to the low loading of Cu/Cu_2O, the two absorption peaks were blurred. Fig. 2(b) showed that the loading of Cu/Cu_2O nanoparticles with different masses did not affect the chemical structure of NH_2-MIL-88B (Fe). The FT-IR characterization results combined with the analysis of the crystal plane data of Cu_2O and Cu^0 in XRD confirmed the successful preparation of Cu/Cu_2O/NH_2-MIL-88B (Fe).

SEM, TEM, and HRTEM were used to observe the morphological characteristics of the original NH_2-MIL-88B (Fe) and Cu/Cu_2O/NH_2-MIL-88B (Fe). Fig. 3(a) and (b) were the SEM images of NH_2-MIL-88B (Fe) and Cu/Cu_2O/NH_2-MIL-88B (Fe), respectively. It could be clearly observed that NH_2-MIL-88B (Fe) was spindle-shaped, with a length of 1.0 to 1.5 μm and a width of 300 to 400 nm.[37] This was consistent with the literature characterization results. Compared with NH_2-MIL-88B (Fe), Cu/Cu_2O loading did not change the morphology of NH2-MIL-88B (Fe), and the complete crystal structure of NH_2-MIL-88B (Fe) was remained in Cu/Cu_2O/NH_2-MIL-88B (Fe). Fig. 3(c) and (d) were

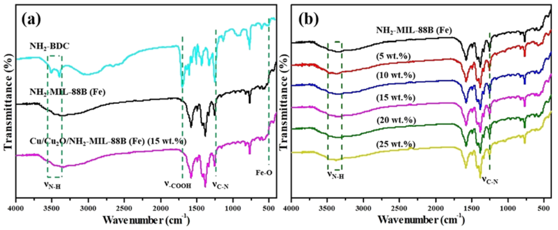

Fig. 2 FT-IR spectra of NH_2-MIL-88B (Fe) and Cu/Cu_2O/NH_2-MIL-88B (Fe) samples (a) and Cu/Cu_2O/NH_2-MIL-88B (Fe) with different loadings (b).

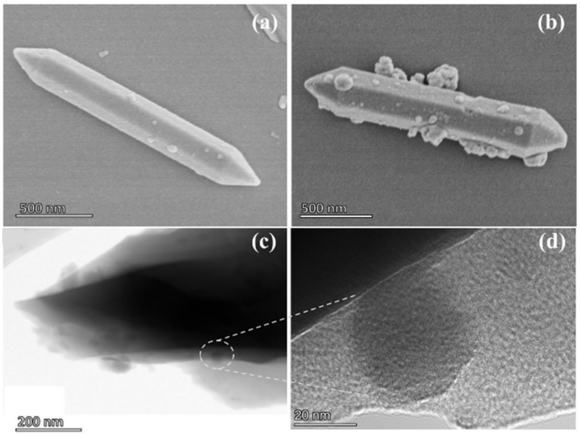

Fig. 3 SEM image of NH_2-MIL-88B (Fe) (a); SEM image (b), TEM image (c), HRTEM image (d) of Cu/Cu_2O/NH_2-MIL-88B (Fe).

the TEM and HRTEM images of Cu/Cu_2O/NH_2-MIL-88B (Fe). It could be observed that the spherical Cu/Cu_2O particles were tightly anchored on the surface of NH_2-MIL-88B (Fe) to form a heterogeneous structure, which was mutually corroborated by the characterization results of XRD and FT-IR. Fig. S1† was the mapping diagram of the material. The analysis showed that C, N, O and Fe were uniformly distributed in the selected spindle-shaped structure. In addition, Cu did not show obvious spindle shape or spherical shape, which might be due to the low quality of Cu and the influence of the test conditions. BET characterization of related materials was showed in Table S1.† The results showed that, compared with NH_2-MIL-88B (Fe), the specific surface area of Cu/Cu_2O/NH_2-MIL-88B (Fe) (15 wt%) was reduced by 94.65 m^2 g^{-1}. It was caused by the loading of Cu/Cu_2O blocking part of the pores of NH_2-MIL-88B (Fe).

In order to clarify the chemical composition and oxidation state of the catalyst, the XPS characterization of Cu/Cu_2O/NH_2-MIL-88B (Fe) (15 wt%) was tested and the results (Fig. 4 and Table S2†) were analyzed and illustrated. The XPS full spectrum shown in Fig. 4(a) clearly showed that there were five elements in the catalyst, corresponding to C 1s, N 1s, O 1s, Fe 2p and Cu 2p, respectively. Fig. 4(b)–(d) deeply analyzed the high-resolution XPS spectra of each element and confirm the existence of important chemical bonds. The XPS spectrum of C 1s could be divided into three peaks, and their respective binding energies were 284.5, 285.5 and 288.4 eV. Among them, the characteristic peak at 284.5 eV represents C=C in the benzene ring skeleton, 285.5 eV and 288.4 eV represent the C–N of –NH_2 and the C=O of –COOH connected to the benzene ring skeleton of the organic ligand, respectively, which was in line with the work of Feng *et al.*[38] Fig. S2(a)† showed the N 1s peak, where the strong peak at 399.2 eV was attributed to –NH_2 connected to the benzene. Fig. S2(b)† was the XPS spectrum of O 1s, in which 531.0 eV was attributed to Fe–O formed by the coordination of –COOH and Fe in NH_2-MIL-88B (Fe), and 531.9 eV was attributed to C–O in –COOH. Fig. S3† was the XPS spectrum of Fe 2p, which corresponded to the Fe–O clusters produced by the coordination of carboxyl groups with Fe. Among them, 717.4 eV was the satellite peak of Fe(III).[39] Fe(III) was the main form of Fe in Cu/Cu_2O/NH_2-MIL-88B (Fe). The main peaks were located at 711.5 eV and 725.0 eV, corresponding to Fe $2p_{3/2}$ and Fe $2p_{1/2}$, respectively. According to Fig. 4(c), it could be observed that the Fe peak in the composite material was negatively shifted. This phenomenon was due to the close contact between Cu/Cu_2O and NH_2-MIL-88B (Fe) to form a heterojunction. Then, the electrons were transferred from Cu/Cu_2O to NH_2-MIL-88B (Fe), which enhanced the electron density of Fe.[40] Fig. 4(d) was the XPS spectrum of Cu 2p, where 941.6 eV was the satellite peak of Cu. The peak positions of the Cu 2p XPS spectrum showed that Cu mainly existed in the form of Cu_2O, and the main peak positions were 934.1 and 935.9 eV, corresponding to Cu $2p_{3/2}$ and Cu $2p_{1/2}$,[41] respectively. However, Cu could also exist in the form of Cu^0. It was difficult to distinguish Cu^0 and Cu_2O because of the close XPS electron orbits of Cu^0 and Cu_2O.[42] Combined the crystal plane data analysis of Cu_2O and Cu^0 in XRD and the results of FT-IR confirmed the successful preparation of Cu/Cu_2O/NH_2-MIL-88B (Fe). The relative mass percentage content of elements (C, N, O, Fe and Cu) on the surface of the catalyst was calculated from the core energy peak areas of C 1s, N 1s, O 1s, Fe 2p and Cu 2p. As shown in Table S2,† the calculated mass fraction of Cu in Cu/Cu_2O/NH_2-MIL-88B (Fe) (15 wt%) was 11.09 wt%, which might be due to the small size of Cu/Cu_2O nanoparticles deposited in the NH_2-MIL-88B (Fe) hole uniformly, resulting in undetectable results (X-ray penetration depth was about 10 nm).[34] In addition, Fig. S4† showed the calculated VB (the valence band) of Cu/Cu_2O/NH_2-MIL-88B (Fe) (15 wt%) was 1.35 eV.

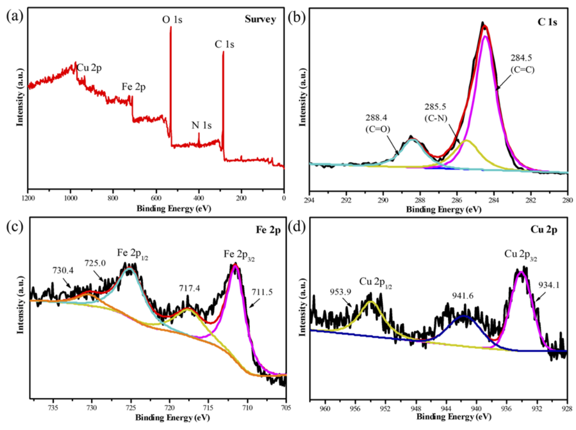

Fig. 4 XPS spectra of Cu/Cu_2O/NH_2-MIL-88B (Fe) (15 wt%) samples (a) survey; (b) C 1s; (c) Fe 2p; (d) Cu 2p, respectively.

In order to investigate the visible light responsiveness of the catalyst and its band gap, the material was characterized by DRS. In Fig. 5(a), the absorbance of Cu/Cu_2O-loaded MOFs in the wavelength range of 420 nm to 800 nm was significantly higher than that of NH_2-MIL-88B (Fe). The better light absorption and responsiveness of composite MOFs in the visible light region was due to the good photosensitivity of Cu_2O and the SPR effect of Cu. Fig. 5(b) was the comparison of the band gap between NH_2-MIL-88B (Fe) and Cu/Cu_2O/NH_2-MIL-88B (Fe). It could be observed that the composite MOFs showed smaller band gap. The excellent photocatalytic performance of MOFs was related to the band gap of MOFs: under the irradiation of incident light, electrons in VB absorbed energy and migrated to CB through E_g to form e^-–h^+ pairs, and then e^-–h^+ pairs migrated to the surface of MOFs to perform photocatalytic reduction and oxidation reactions. Therefore, a smaller band gap helped to excite more electrons, which helped to improve

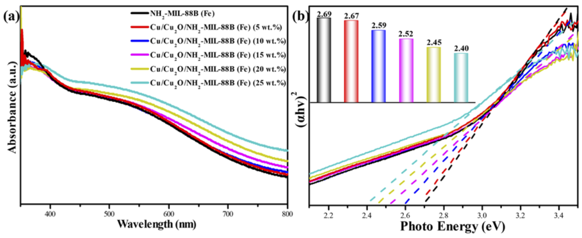

Fig. 5 DRS spectra (a) and the band gaps (b) of NH_2-MIL-88B (Fe) and Cu/Cu_2O/NH_2-MIL-88B (Fe) samples.

the photocatalytic performance. The band gaps of different loadings of $Cu/Cu_2O/NH_2$-MIL-88B (Fe) were 2.67 eV, 2.59 eV, 2.52 eV, 2.45 eV, 2.40 eV, which were all lower than the 2.69 eV of NH_2-MIL-88B (Fe). It indicated that heterojunction MOFs might have better catalytic performance. In addition, the VB of $Cu/Cu_2O/NH_2$-MIL-88B (Fe) (15 wt%) tested in XPS was 1.35 eV, and the CB of $Cu/Cu_2O/NH_2$-MIL-88B (Fe) (15 wt%) was −1.17 eV.

3.2 Photocatalytic activities

In order to investigate the photocatalytic activity of the catalyst, taking Cr(VI) in water as the target and driven by visible light, the photocatalytic degradation ability of $Cu/Cu_2O/NH_2$-MIL-88B (Fe) on water pollutants was investigated. Fig. 6 showed the reduction effect of the catalyst on Cr(VI) in water under different reaction conditions. The black part in the reduction efficiency histogram represented the adsorption rate, and the colored part represented the reduction rate. Through the test, the concentration of the Cr(VI) solution only decreased in a short time in the reduction system without light irradiation conditions due to the adsorption of the catalyst. The solution concentration basically no longer changed after reaching the adsorption–desorption equilibrium. In addition, when there was no catalyst, the increase in the concentration of the Cr(VI) solution was caused by amount of evaporation of the reaction solution caused by the prolonged exposure of the xenon lamp. The above two catalytic effects indicated that visible light irradiation and the presence of catalysts were indispensable for the photocatalytic reduction of Cr(VI). The photocatalytic adsorption reduction rate of $Cu/Cu_2O/NH_2$-MIL-88B (Fe) (15 wt%) introduced by Cu/Cu_2O nanoparticles reached 96.3%, which was 1.39 times that of NH_2-MIL-88B (Fe). Fig. 6(b) showed the fitting relationship of the photocatalytic reaction kinetics of the catalyst. The photocatalytic reaction was linear relationship with time. The catalytic kinetic rate constant k and the fitting coefficient R^2 were shown in the Table S3.† The kinetic rate constant followed $Cu/Cu_2O/NH_2$-MIL-88B (Fe) (15 wt%) > NH_2-MIL-88B (Fe) > no light > no catalyst.

The experimental results of the photocatalytic performance test showed that the introduction of amino groups and the loading of Cu/Cu_2O nanoparticles could effectively improve the photocatalytic performance of NH_2-MIL-88B (Fe). Therefore, in order to explore the factors that affect the photocatalytic reduction effect and screen out the best reaction conditions of $Cu/Cu_2O/NH_2$-MIL-88B (Fe), we had investigated the various conditions of the reaction system. Fig. 7(a) showed the investigation of the photocatalytic adsorption reduction effect of different loadings of $Cu/Cu_2O/NH_2$-MIL-88B (Fe). The results showed that as the loading of Cu/Cu_2O nanoparticles increasing, the photocatalytic effect showed an increasing trend, and the loading of 15 wt% was the best; however, as the load continued to increase, the catalytic effect decreased to varying degrees. It was due to the more Cu/Cu_2O nanoparticles blocked part of the pore structure of NH_2-MIL-88B (Fe), which losed more reactive sites. Fig. 7(b) examined the effect of pH on the photocatalytic effect, which showed that 2 was the optimal pH condition. In aqueous solution, Cr exists in five forms: CrO_4^{2-}, $Cr_2O_7^{2-}$, $HCrO_4^-$, $HCr_2O_7^{2-}$ and H_2CrO_4, the specific form depends mainly on the pH value. When pH = 2, the Cr(VI) in the solution existed in the form of $Cr_2O_7^{2-}$. When the pH value was adjusted below 5, Cr(VI) existed in the form of $HCrO_4^-$. When the pH became smaller and smaller, the zeta potential changed from negative to positive, and H^+ in the solution will promote the conversion of Cr(VI) to Cr(III). Thereby it was more conducive to the adsorption and reduction.[43] In addition, the generated Cr(III) easily combines with OH^- to form insoluble $Cr(OH)_3$ attached to the surface of the catalyst when the pH value was higher, thereby occupying effective photocatalytic active sites and hindering subsequent reactions. The reaction formula of photocatalytic reduction of Cr(VI) under different pH conditions was as follows:

$$\begin{aligned}&Cu/Cu_2O/NH_2\text{-MIL-88B (Fe)} \rightarrow \\ &\qquad Cu/Cu_2O/NH_2\text{-MIL-88B (Fe)} + e^- + h^+\end{aligned} \quad (1)$$

$$14H^+ + Cr_2O_7^{2-} + 6e^- \rightarrow 2Cr^{3+} + 7H_2O \quad (2)$$

$$7H^+ + HCrO_4^- + 3e^- \rightarrow Cr^{3+} + 4H_2O \quad (3)$$

Fig. 7(c) investigated the effect of catalyst concentration on the adsorption and reduction efficiency of Cr(VI) in water. The

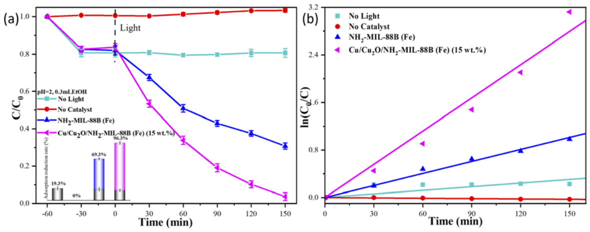

Fig. 6 Photocatalytic reduction efficiency diagram of Cr(VI) under visible light conditions (a) and the fitting of the pseudo-first-order linear line for the photocatalytic reaction (b).

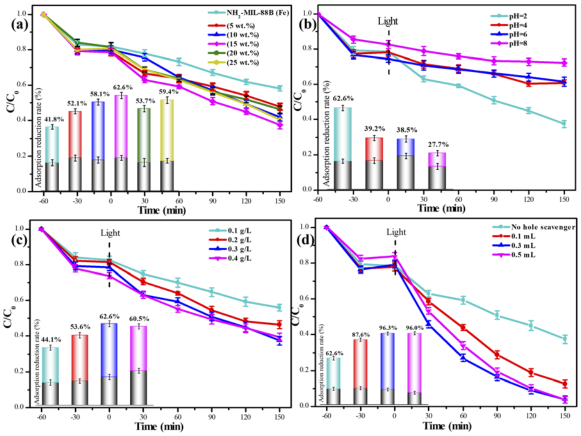

Fig. 7 Photocatalytic reduction efficiency diagram of $Cu/Cu_2O/NH_2$-MIL-88B (Fe) samples to Cr(VI) under different conditions (a) different Cu/Cu_2O loading, (b) pH values, (c) different concentration of $Cu/Cu_2O/NH_2$-MIL-88B (Fe), (d) ethanol addition.

results showed that in the dark reaction part, with the increase of the amount of catalyst, the adsorption capacity of Cr(VI) in water increased gradually and the reduction effect was better and better. However, with the increase of concentration, the reaction effect gradually decreased. This is because when too many catalyst particles are suspended in the reaction system, a large amount of incident light will be shielded, resulting in a decrease in the reduction effect. Hole trapping agent is an additive that is used to consume h^+ after the formation of photogenerated e^-–h^+ pairs in the catalytic reaction system, thereby inhibiting the recombination of photogenerated carriers and improving the photocatalytic efficiency.[44] In the catalytic reaction system, the addition of an appropriate amount of hole trapping agent can effectively improve the reduction rate of pollutants in water by the catalyst. Ethanol as hole trapping agent had a stable structure, non-toxic, cheap and easy to obtain. Based on the above conditions, the influence of the amount of ethanol on the efficiency of adsorption and reduction was investigated. Fig. 7(d) showed the effect of different amounts of ethanol on $Cu/Cu_2O/NH_2$-MIL-88B (Fe) (15 wt%) photocatalytic adsorption and reduction of Cr(VI) in water. It could be observed that the amount of ethanol added was from 0 to 0.3 mL, the photocatalytic adsorption reduction rate was getting higher and higher, but the adsorption reduction rate did not change significantly when the addition amount was increased to 0.5 mL.

Therefore, after the above tests, the optimum conditions for photocatalytic adsorption and reduction of Cr(VI) by $Cu/Cu_2O/NH_2$-MIL-88B (Fe) can be summarize: the catalyst is $Cu/Cu_2O/NH_2$-MIL-88B (Fe) (15 wt%), the solution pH is 2, the catalyst concentration is 0.3 g L^{-1}, and 0.3 mL of ethanol is added. The photocatalytic adsorption and reduction rate of Cr(VI) in water reaches 96.3%.

3.3 Reusability and stability

In order to investigate the cyclic reduction ability of the catalyst and its own recycling stability, a cyclic experiment test was carried out on $Cu/Cu_2O/NH_2$-MIL-88B (Fe) (15 wt%). The reacted catalyst was collected, washed with ethanol, and then dried under vacuum at 70 °C overnight, and then the ground catalyst was repeated the above performance test process. Fig. 8 showed the cyclic reduction performance test of the catalyst for Cr(VI) in water: after three cycles, the catalyst still showed good photocatalytic performance, and its reduction efficiency still reaches 88.9%. Fig. S5† showed the XRD and FT-IR characterization of the catalyst after recycling. The results showed that the crystal structure and chemical structure of the catalyst did not change significantly before and after use, indicating that the catalyst has good recycling practicability.

4. Photocatalytic mechanism

According to the above analysis, the possible mechanism of $Cu/Cu_2O/NH_2$-MIL-88B (Fe) photocatalytic reduction of Cr(VI) in water is proposed. As shown in Fig. 9, when $Cu/Cu_2O/NH_2$-MIL-88B (Fe) is irradiated with visible light, the electrons of NH_2-MIL-88B (Fe) ($E_g = 2.6$ eV) absorbed energy, excited and transition from VB to CB, thereby obtaining a short e^-–h^+, Cu/Cu_2O improved its light absorption ability and produced more photogenerated carriers to participate in the photocatalytic process. Cu^0 has SPR effect, which can produce e^-–h^+ to participate in the reaction after absorbing visible light. On the other hand, the e^- of Cu_2O ($E_g = 2.1$ eV)[34] excited under visible light can be transferred to CB of NH_2-MIL-88B (Fe) through heterojunction and Cu nanoparticles, reducing the Cr(VI) adsorbed on the catalyst surface to Cr(III). As shown in Fig. S6,† when $AgNO_3$ and 2,6-di-*tert*-butyl-4-methylphenol were added as trapping agents for e^- and $^{\cdot}O_2^-$, the efficiency of photocatalytic reduction of Cr(VI) decreased significantly, the active species in the system are e^- and $^{\cdot}O_2^-$. The electrons transferred to NH_2-MIL-88B (Fe) react with O_2 in water to generate $^{\cdot}O_2^-$, which are used to reduce Cr(VI) to Cr(III). At the same time, the h^+ on NH_2-MIL-88B (Fe) is accelerated to transfer to Cu_2O nanoparticles by Cu nanoparticles through heterojunction under the action of built-in electric field,[45] and oxidizes the ethanol adsorbed on the catalyst surface to generate oxidation products. During the period, the existence of Cu nanoparticles not only effectively transfers the photogenerated carriers of Cu_2O and NH_2-MIL-88B (Fe), inhibits the recombination of photogenerated e^-–h^+, but also accelerates the transfer of photogenerated carriers. In addition, the existence of the hole trapping agent effectively consumes

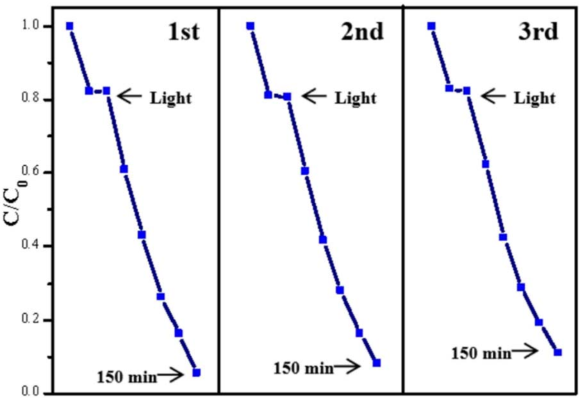

Fig. 8 Reusability for photocatalytic reduction of Cr(VI).

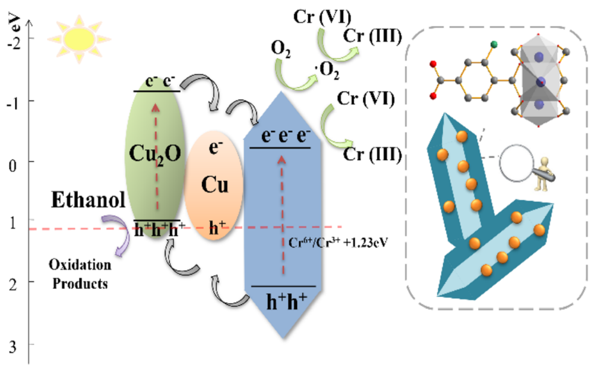

Fig. 9 Possible mechanism diagram of photocatalytic reduction of Cr(VI) on $Cu/Cu_2O/NH_2$-MIL-88B (Fe).

the photogenerated h^+, reduces the recombination rate of photogenerated carriers,[46] and enables the photogenerated electrons to be effectively input into the reaction process of reducing Cr(VI) to Cr(III).

5. Conclusions

Using the strategy of constructing heterostructure, the Cu/Cu_2O/NH_2-MIL-88B (Fe) photocatalyst was prepared by solvothermal method and light-assisted reduction method. The loading of Cu_2O effectively improved the visible light absorption capacity of the composite material and reduced the band gap. The SPR effect of Cu promoted the separation and transfer of photogenerated carriers. The photocatalytic performance test showed that the photocatalytic adsorption reduction rate of Cu/Cu_2O/NH_2-MIL-88B (Fe) (15 wt%) on Cr(VI) reached 96.3% after the reaction for 150 min, which was NH2-MIL-88B (Fe) 1.39 times. This was due to the transfer of photogenerated electrons generated by Cu_2O to NH_2-MIL-88B (Fe) through the heterojunction, thereby promoting the separation of photogenerated carriers. In addition, studies had shown that Cu/Cu_2O/NH_2-MIL-88B (Fe) (15 wt%) had good stability and recyclability.

Data availability

The data supporting this article have been included as part of the ESI.†

Conflicts of interest

There are no conflicts to declare.

Acknowledgements

This work was supported by the Scientific Research Foundation of Education Department of Liaoning Province of China (No. LJ212410845006) and Scientific Research and Innovation team Project of Dalian Vocational and Technical College (2024).

Notes and references

1 M. Müller, S. Hermes, K. Kähler, M. W. E. van den Berg, M. Muhler and R. A. Fischer, *Chem. Mater.*, 2008, **20**, 4576–4587.
2 Z. Shi, Y. Zhang, G. Duoerkun, W. Cao, T. Liu, L. Zhang, J. Liu, M. Li and Z. Chen, *Environ. Sci.: Nano*, 2020, **7**, 2708–2722.
3 D. Yang, W. Fang, H. Zhang, H. Sun, X. Gu, H. Chen and J. Luo, *J. Hazard. Mater.*, 2024, **476**, 134985.
4 N. Senamart, K. Deekamwong, J. Wittayakun, S. Prayoonpokarach, N. Chanlek, Y. Poo-arporn, S. Wannapaiboon, P. Kidkhunthod and S. Loiha, *RSC Adv.*, 2022, **12**, 25578–25586.
5 N. S. Jamaluddin, N. H. Alias, S. Samitsu, N. H. Othman, J. Jaafar, F. Marpani, W. J. Lau and Y. Z. Tan, *J. Environ. Chem. Eng.*, 2022, **10**, 108665.
6 P. Xu, S. Huang, Y. Lv, Y. Chen, M. Liu and H. Fan, *RSC Adv.*, 2018, **8**, 5749–5759.
7 D. S. Raie, I. Tsonas, M. Canales, S. Mourdikoudis, K. Simeonidis, A. Makridis, D. Karfaridis, S. Ali, G. Vourlias, P. Wilson, L. Bozec, L. Ciric and N. T. Kim Thanh, *Nanoscale Adv.*, 2023, **5**, 2897–2910.
8 A. Bhati, S. R. Anand, D. Saini, Gunture and S. K. Sonkar, *npj Clean Water*, 2019, **2**, 12.
9 Y. Fei, S. Chen, Z. Wang, T. Chen and B. Zhang, *J. Environ. Manage.*, 2022, **324**, 116298.
10 Y. Luo, Y. Lan, X. Liu, M. Xue, L. Zhang, Z. Yin, X. He, X. Li, J. Yang, Z. Hong, M. Naushad and B. Gao, *Sep. Purif. Technol.*, 2023, **317**, 123926.
11 Z. Fan, Q. Zhang, B. Gao, M. Li, C. Liu and Y. Qiu, *Chemosphere*, 2019, **217**, 85–94.
12 C. Zhang, Q. Zhuang, H. Wang, X. Ying, R. Ji, D. Sheng, W. Dong and A. Xie, *J. Colloid Interface Sci.*, 2023, **630**, 235–248.
13 J. Ma, L. Li, Y. Zhang, J. Qian and X. Wang, *Chin. J. Struct. Chem.*, 2024, **43**, 100466.
14 X. Wu, G. Chen, L. Li, J. Wang and G. Wang, *J. Mater. Sci. Technol.*, 2023, **167**, 184–204.
15 A. Helal, S. Shaheen Shah, M. Usman, M. Y. Khan, M. A. Aziz and M. Mizanur Rahman, *Chem. Rec.*, 2022, **22**, e202200055.
16 L. Xia, W. Zhou, Y. Xu, Z. Xia, X. Wang, Q. Yang, G. Xie, S. Chen and S. Gao, *Chem. Eng. J.*, 2023, **451**, 138747.
17 X.-P. Wu, L. Gagliardi and D. G. Truhlar, *J. Am. Chem. Soc.*, 2018, **140**, 7904–7912.
18 H. He, X. Wang, Q. Yu, W. Wu, X. Feng, D. Kong, X. Ren and J. Gao, *Catalysts*, 2023, **13**, 876.
19 X.-S. Wang, C.-H. Chen, F. Ichihara, M. Oshikiri, J. Liang, L. Li, Y. Li, H. Song, S. Wang, T. Zhang, Y.-B. Huang, R. Cao and J. Ye, *Appl. Catal., B*, 2019, **253**, 323–330.
20 S. Mandal, S. Natarajan, P. Mani and A. Pankajakshan, *Adv. Funct. Mater.*, 2020, **31**, 2006291.
21 Z. Zhao, H. Zhao, X. Du and X. Zhang, *Surf. Interfaces*, 2024, **46**, 104079.
22 Q. Zhang, J.-B. Liu, L. Chen, C.-X. Xiao, P. Chen, S. Shen, J.-K. Guo, C.-T. Au and S.-F. Yin, *Appl. Catal., B*, 2020, **264**, 118529.
23 Y.-X. Jing, M.-M. Suo, G.-P. Yang and Y.-Y. Wang, *Inorg. Chem.*, 2023, **62**, 6361–6367.
24 L. Shi, T. Wang, H. Zhang, K. Chang, X. Meng, H. Liu and J. Ye, *Advanced Science*, 2015, **2**, 1500006.
25 Y. Zeng, X. Li, Y. Chen and S. Li, *ACS Omega*, 2023, **8**, 36978–36985.
26 Y. Liu, S. Huang, X. Huang and D. Ma, *Mater. Horiz.*, 2024, **11**, 1611–1637.
27 T. Xie, F. Li, P. Song, M. Fang, L. Duan, Q. Zhang and W. Geng, *J. Alloys Compd.*, 2024, 1002.
28 Z. Wang, C. Zhu, Z. Ni, H. Hojo and H. Einaga, *ACS Catal.*, 2022, **12**, 14976–14989.
29 P. Liu, A. Dörfler, A. A. Tabrizi, L. Skokan, D. Rawach, P. Wang, Z. Peng, J. Zhang, A. P. Ruediger and J. P. Claverie, *ACS Appl. Mater. Interfaces*, 2023, **15**, 27832–27844.

30 L. Chen, J. Lei, L. Tian, K. Deng and G. Cheng, *Ceram. Int.*, 2021, **47**, 23001–23013.

31 S. F. U. Farhad, D. Cherns, J. A. Smith, N. A. Fox and D. J. Fermín, *Mater. Des.*, 2020, 193.

32 R. Yuan, C. Yue, J. Qiu, F. Liu and A. Li, *Appl. Catal., B*, 2019, **251**, 229–239.

33 D. Xie, Y. Ma, Y. Gu, H. Zhou, H. Zhang, G. Wang, Y. Zhang and H. Zhao, *J. Mater. Chem. A*, 2017, **5**, 23794–23804.

34 I. Majeed, M. A. Nadeem, A. Badshah, F. K. Kanodarwala, H. Ali, M. A. Khan, J. A. Stride and M. A. Nadeem, *Catal. Sci. Technol.*, 2017, **7**, 677–686.

35 M. Müller, S. Hermes, K. Kähler, M. W. E. van den Berg, M. Muhler and R. A. Fischer, *Chem. Mater.*, 2008, **20**, 4576–4587.

36 M. Yadollahi, H. Hamadi and V. Nobakht, *J. Hazard. Mater.*, 2020, **399**, 122872.

37 H. Ma, B. Yu, Q. Wang, G. Owens and Z. Chen, *J. Colloid Interface Sci.*, 2021, **583**, 279–287.

38 X. Feng, R. Long, C. Liu and X. Liu, *Sep. Purif. Technol.*, 2022, **302**, 122138.

39 R. Yuan, C. Yue, J. Qiu, F. Liu and A. Li, *Appl. Catal., B*, 2019, **251**, 229–239.

40 M.-Y. Lan, Y.-H. Li, C.-C. Wang, X.-J. Li, J. Cao, L. Meng, S. Gao, Y. Ma, H. Ji and M. Xing, *Nat. Commun.*, 2024, **15**, 7208.

41 K. Müller, J. Wadhwa, J. Singh Malhi, L. Schöttner, A. Welle, H. Schwartz, D. Hermann, U. Ruschewitz and L. Heinke, *Chem. Commun.*, 2017, **53**, 8070–8073.

42 M. C. Biesinger, L. W. M. Lau, A. R. Gerson and R. S. C. Smart, *Appl. Surf. Sci.*, 2010, **257**, 887–898.

43 Z. Lv, X. Tan, C. Wang, A. Alsaedi, T. Hayat and C. Chen, *Chem. Eng. J.*, 2020, **389**, 123428.

44 Z. Yu, F. Zhu, T. Chen, J. Li, Q. Feng, F. Yang and X. Zhang, *J. Photochem. Photobiol., A*, 2023, **440**, 114637.

45 S. Zhu, X. Chen, Z. Li, X. Ye, Y. Liu, Y. Chen, L. Yang, M. Chen, D. Zhang, G. Li and H. Li, *Appl. Catal., B*, 2020, **264**, 118515.

46 F. Xu, R. D. Webster, J. Chen, T. T. Y. Tan, P. H. L. Sit and W. Y. Teoh, *Appl. Catal., B*, 2017, **210**, 444–453.